Comparing UNet and HRNet for Geomorphic Feature Extraction from Digital Terrain Model-Derived Land Surface Parameters

Behnam Solouki [1*], Aaron E. Maxwell [1]
[1]West Virginia University Department of Geology and Geography, Morgantown, WV, USA
[*]Correspondence: bs00135@mix.wvu.edu

Paper is a non-peer reviewed preprint submitted to EarthArXiv.

Abstract

Automated extraction of geomorphic features from high spatial resolution terrain data is important for environmental monitoring, geohazard assessment, and landscape change analysis. This study compares two convolutional neural network architectures, UNet and High-Resolution Network (HRNet), for semantic segmentation of mine benches and sinkholes from lidar-derived digital terrain models and land surface parameters. Mine benches represent anthropogenic, elongated, stepped landforms associated with historic surface mining, whereas sinkholes are natural, compact depressions common in karst terrain. Three terrain-derived input layers were used: square-root-transformed slope, broad-scale topographic position index, and fine-scale annulus topographic position index. Models were trained using five training sample sizes, including 50, 100, 250, 500, and 1,000 chips, and evaluated using overall accuracy, precision, recall, and F1-score. Results suggest that both architectures achieved broadly comparable segmentation performance, with F1-scores generally improving as training sample size increased. HRNet showed a practically notable advantage for sinkholes at the smallest sample size, but this advantage diminished as more training data were provided. For mine benches, UNet and HRNet performed similarly across most sample sizes, with neither architecture showing a consistent advantage. Although HRNet had substantially greater computational complexity, requiring approximately 12.7 times more trainable parameters and about three times more FLOPs and MACs than UNet, this additional cost did not produce a corresponding accuracy gain. These findings indicate that, for terrain-only geomorphic feature extraction, baseline UNet offers a highly efficient and competitive solution, while HRNet may be useful in limited-data settings or for features requiring high spatial resolution spatial preservation.

1. Introduction

Understanding and mapping Earth surface features is critical for monitoring environmental change, managing natural hazards, and assessing the impacts of human activity. In particular, geomorphic feature extraction has become an increasingly important task in the geosciences. Traditionally, this process has relied on expert-driven, manual interpretation of aerial photographs or terrain models. However, the rapid expansion of high spatial resolution elevation data derived from light detection and ranging (lidar) and the evolution of deep learning–based semantic segmentation techniques offer new opportunities to automate and scale geomorphic mapping. One subset of landforms that has received growing attention in geomorphic and environmental research is anthropogenic geomorphic features, or those shaped or created by human activity. These include mine benches, which result from surface mining operations, and are often associated with slope instability, erosion, and altered hydrological patterns [1]. In contrast, sinkholes are naturally occurring geomorphic features that form through subsurface dissolution of soluble rocks, particularly in karst terrains. They pose serious geohazard and water quality risks and are of increasing concern in many developed regions due to their potential for sudden ground collapse [2]. Despite their distinct origins, both mine benches and sinkholes represent spatially complex, irregular features that are challenging to detect and delineate, especially using traditional classification methods that depend on multispectral imagery. These features may appear spectrally homogeneous or indistinguishable from their surroundings in aerial or satellite imagery, yet they often have distinct topographic expressions when observed in digital terrain models (DTMs).

The emergence of convolutional neural networks (CNNs), especially fully convolutional architectures such as UNet [3] and High-Resolution Network (HRNet) [4], has significantly improved the performance of automated landform classification. These models are capable of learning complex spatial patterns and context from multiband raster inputs, such as land surface parameters (LSPs) derived from lidar DTMs. While UNet follows an encoder-decoder architecture with skip connections to recover fine spatial detail, HRNet maintains high spatial resolution representations across multiple branches and fuses them continuously, enabling both local feature extraction and global contextual reasoning. These differences in architecture and information flow are likely to influence model performance depending on the spatial complexity, scale, and morphology of the target geomorphic features. Previous research has documented that UNet variants can successfully map anthropogenic landforms such as terraces, valley fills, and mine benches from terrain data alone [5-7]. Similarly, HRNet-based models have demonstrated strong performance in preserving spatial detail and detecting features with complex boundaries in urbanized landscapes [8-10]. However, no prior studies have systematically compared these two architectures within a terrain-only deep learning framework across multiple geomorphic feature types and evaluated how model performance varies across features with different geomorphic signatures, such as the linear, stepped geometry of mine benches versus the circular depressions of sinkholes. This knowledge gap limits our ability to generalize or optimize models for diverse real-world applications in geomorphic hazard monitoring, terrain change analysis, and environmental regulation compliance.

This research addresses these gaps by developing and evaluating deep learning models for the semantic segmentation of mine benches and sinkholes using LSPs generated from lidar-based DTMs. Specifically, the study compares UNet and HRNet architectures to assess their relative performance across feature types with contrasting morphology. The models are trained and tested using labeled datasets derived from known sinkhole inventories and mapped historic mining extents. In addition to measuring segmentation accuracy, this study evaluates the models' ability to generalize across datasets, their sensitivity to different sample sizes, and their computational efficiency. These insights contribute to the development of optimized, terrain-based segmentation workflows for geospatial applications requiring accurate feature extraction from high spatial resolution elevation data.

2. Research Objectives

The overarching goal of this study is to compare the performance of baseline UNet and HRNet deep learning models for the semantic segmentation of geomorphic features, specifically mine benches and sinkholes, using lidar-derived terrain data. To achieve this goal, after preprocessing and preparing geomorphic feature datasets, I first implement and train baseline UNet and HRNet models using consistent training pipelines and hyperparameters to ensure a fair comparison. Next, I evaluate model performance across varying training sample sizes (50, 100, 250, 500, and 1,000) to examine how data availability influences learning outcomes and to assess model robustness under limited-data conditions. Then, I compare the models' segmentation accuracy using standard evaluation metrics, including overall accuracy, precision, recall, and F1-score. Finally, I assess and report computational efficiency, including parameter counts, FLOPs (floating point operations), and MACs (Multiply-Accumulate Operations), to evaluate the practicality of each model for potential deployment in resource-constrained environments. This study tests the following hypotheses:

- **H1:** HRNet outperforms UNet in segmentation accuracy across both mine benches and sinkholes, due to its ability to maintain high spatial resolution representations and continuously integrate multiscale context.
- **H2:** Model performance varies by feature type; HRNet demonstrates particular advantages for irregular or fine-scale features (e.g., sinkholes) due to its high spatial resolution feature preservation, while UNet may perform competitively on structured features (e.g., mine benches) that benefit from its encoder–decoder design.
- **H3:** Both models are expected to benefit from increased training sample sizes. However, model performance at smaller sample sizes may differ: HRNet's architectural complexity could lead to overfitting under limited data conditions, while UNet's simpler encoder–decoder design may offer greater stability.

3. Background

3.1. Geospatial Semantic Segmentation

Semantic segmentation refers to the process of assigning a class label to each pixel in an image, enabling dense, fine-grained prediction of spatial categories [11, 12]. In the context of remote sensing and geographic analysis, geospatial semantic segmentation extends this task to the classification of pixels in spatially referenced raster datasets such as satellite imagery, lidar-derived products, or multispectral or multitemporal composites. Unlike traditional classification methods that treat pixels independently or in tabular form, semantic segmentation models consider the spatial context and morphological structure of landscape features, making them especially well-suited for complex mapping tasks involving natural and anthropogenic surface forms [13, 14].

One important domain of geospatial semantic segmentation is geomorphic mapping, which involves identifying landforms based on their shape, structure, texture, and topographic context. These features may be natural, such as sinkholes, river terraces, and landslides, or anthropogenic, such as mine benches, agricultural terraces, and valley fills. The latter have garnered growing attention due to their widespread alteration of terrain and association with environmental risks like erosion, slope instability, and sedimentation. However, accurately detecting and classifying such features remains a significant challenge due to their irregular morphology and weak spectral contrast, which often render them undetectable in optical imagery. Instead, a growing body of research supports the use of high spatial resolution terrain-based data, particularly from lidar or UAV-derived digital elevation models, for this task. Tarolli et al. [15] proposed a general diagnostic framework for recognizing the "fingerprints" of anthropogenic geomorphic activity embedded in the topography itself, emphasizing the role of slope, curvature, and topographic discontinuities. Müller et al. [16] and Ahmad et al. [17] demonstrated the utility of airborne and UAV-based terrain surface models for quantifying subtle vertical changes and mapping geomorphic hazards such as landslides with high spatial precision. Similarly, Conley et al. [18] documented that topographic thresholds derived from lidar data could effectively predict zones of soil preservation versus erosion, while Chen et al. [19] identified consistent topographic controls, including slope and curvature, governing the distribution of coseismic landslides across diverse earthquake zones. Collectively, these studies underscore that terrain morphology encodes critical information about both natural and human-induced processes, and that leveraging terrain-based inputs can significantly improve the detection and classification of geomorphic features that are otherwise invisible in spectral imagery.

Lidar has revolutionized high spatial resolution topographic mapping, offering dense 3D point cloud data that can be used to derive bare-earth DTMs with spatial resolutions finer than 1 m. DTMs provide elevation values devoid of vegetation or built structures, allowing analysts to examine the terrain surface directly. From these DTMs, a wide range of LSPs can be computed to capture variations in slope, curvature, roughness, and topographic position. These LSPs form a rich set of descriptors that represent geomorphic form and context and have been widely used for manual or semi-automated landform classification. However, traditional rule-based or thresholding approaches often fall short when applied to heterogeneous, complex, or overlapping geomorphic features. This motivates the use of data-driven, deep learning approaches capable of learning spatial patterns directly from LSP inputs.

In this context, deep CNNs are particularly well-suited to the task of geospatial semantic segmentation. CNN-based architectures such as UNet and HRNet can effectively capture local spatial patterns as well as larger contextual structures, enabling them to recognize both the fine-scale geometry of a feature and its broader topographic setting [20]. When applied to multichannel inputs derived from lidar, CNN-based models can learn to distinguish complex anthropogenic features from natural terrain. Importantly, these models do not require handcrafted features or extensive pre-processing; instead, they learn directly from labeled training data, enabling a scalable and flexible approach to geomorphic feature mapping. As the availability of high spatial resolution lidar datasets continues to grow, the integration of deep learning with terrain-based inputs offers a powerful pathway for advancing geomorphic analysis. Geospatial semantic segmentation models trained on lidar-derived LSPs can support the creation of consistent, high spatial resolution inventories of anthropogenic landforms, helping to close critical gaps in environmental monitoring, landscape restoration, and geohazard mitigation.

3.2. UNet

The UNet architecture, first introduced by Ronneberger et al. [3] for biomedical image segmentation, has become one of the most popular deep learning models for pixel-level prediction tasks. What makes UNet especially powerful is its encoder-decoder structure with skip connections (Figure 1). As the input image moves through the encoder, the network captures abstract features and context using a combination of convolutional layers and max pooling operations. Then, in the decoder, it gradually reconstructs the image back to its original spatial resolution. A distinctive feature of UNet is its skip connections, which link corresponding layers in the encoder and decoder to combine deep, abstract features with shallow, spatially detailed ones. This architecture enables precise pixel-level predictions, particularly for objects with fine boundaries or irregular shapes. Due to its ability to balance localization accuracy with contextual awareness, UNet is particularly well-suited for remote sensing applications such as object detection, landform segmentation, and land cover classification.

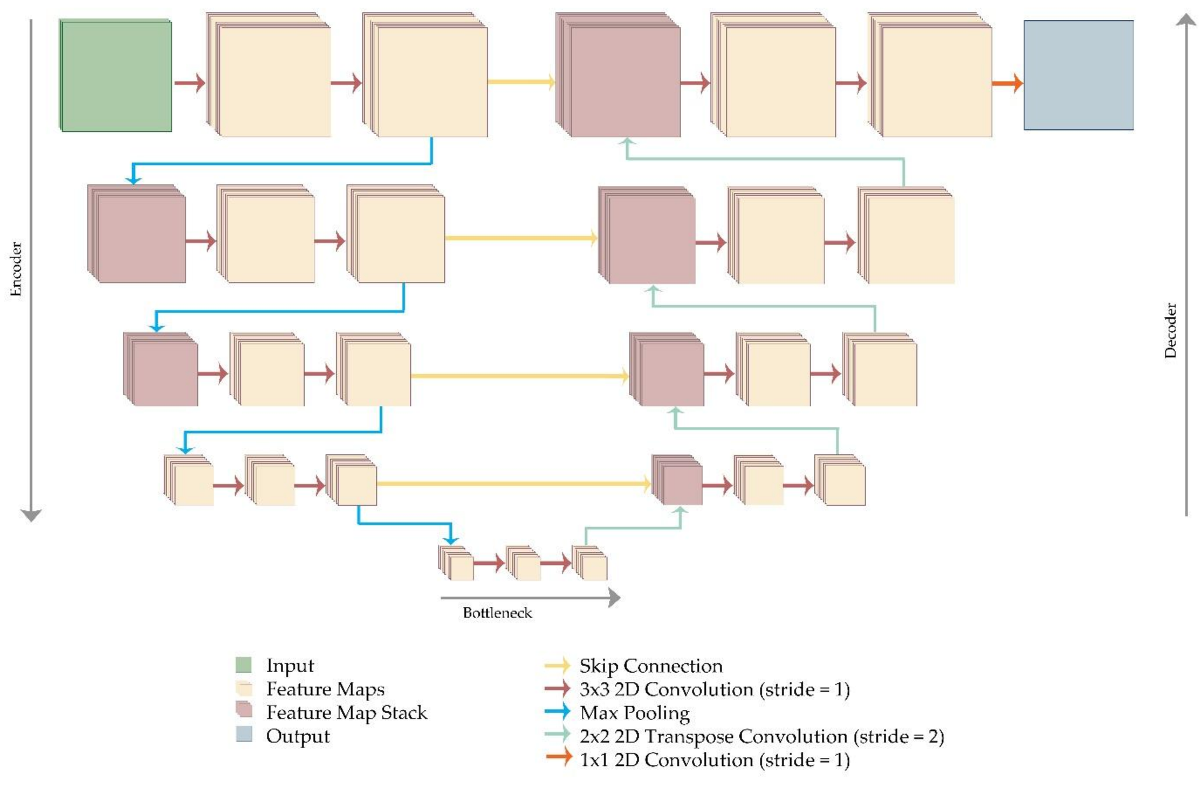

Figure 1. Conceptualization of the UNet architecture [3].

A growing body of literature has demonstrated UNet's effectiveness across a diverse set of geospatial applications, from urban mapping and agricultural monitoring to disaster assessment and environmental change detection. The consistent adoption of UNet in these studies underscores its versatility and robustness, particularly in handling high spatial resolution imagery, class imbalance, and complex spatial patterns. For instance, Prakash et al. [21] used a modified UNet with a ResNet-34 backbone to detect landslides from fused optical and lidar-derived terrain data, finding it outperformed both pixel-based and object-based traditional machine learning approaches in accuracy and spatial consistency. Their integration of focal Tversky loss helped mitigate the effects of class imbalance, an ongoing challenge in geospatial feature segmentation. Similarly, Yi et al. [22] demonstrated that a residualized UNet significantly improved urban building footprint extraction from very high spatial resolution imagery, achieving F1-scores exceeding 0.9 and outperforming object-based image analysis and support vector machine-based methods. Pan et al. [23] applied UNet to both segment and classify buildings in dense urban villages, highlighting its advantages over object-based image analysis and random forest in delineating adjacent structures and producing clean boundaries in high-density areas.

UNet's effectiveness also extends to environmental monitoring and infrastructure mapping. He et al. [24] enhanced UNet with atrous spatial pyramid pooling (ASPP) and structural similarity loss for road extraction, showing that the model could recover finer road structures while maintaining topological coherence. In cryospheric research, Baumhoer et al. [25] employed UNet to extract glacier and ice shelf calving fronts from Sentinel-1 synthetic aperture radar (SAR) data, achieving near-human-level precision across the Antarctic coastline. Their study emphasized the model's generalizability and operational scalability for large-area, time-critical monitoring. Likewise, Freudenberg et al. [26] used UNet for palm tree detection, demonstrating that its segmentation capabilities could be combined with peak detection methods to identify individual trees across thousands of square kilometers with minimal manual effort. In agricultural applications, Onojeghuo et al. [27] proposed a ResU-Net variant, incorporating residual blocks into UNet, for delineating smallholder paddy rice fields using multitemporal Sentinel-1 SAR and Sentinel-2 multispectral data. Their model achieved superior performance in detecting fragmented and irregular field boundaries and demonstrated the benefits of multi-source data fusion within a deep learning framework. Among these efforts, a recent study from our lab by Farhadpour and Maxwell [7] specifically examined UNet's role in extracting anthropogenic geomorphic features. The study systematically compared eight UNet variants for segmenting agricultural terraces, mine benches, or valley fills from the landscape background using lidar-derived LSPs. The study emphasized the interpretability and efficiency of UNet-based models trained solely on terrain-derived inputs, without relying on spectral imagery. Their findings reinforced UNet's flexibility and relevance for pixel-wise geomorphic mapping tasks, particularly when spatial context and shape preservation are crucial. Together, these studies show that UNet remains a strong baseline for remote sensing segmentation, capable of adapting to various data types, spatial scales, and semantic targets. However, they also point to current limitations such as boundary blurring, class imbalance sensitivity, and difficulty capturing long-range dependencies, which motivate exploration of more advanced architectures such as HRNet.

3.3. HRNet

High-resolution network (HRNet), introduced by Wang et al. [4], represents a major shift in CNN design for dense prediction tasks such as semantic segmentation. Unlike conventional encoder-decoder models such as UNet, which downsample input images and then attempt to recover spatial detail during upsampling, HRNet maintains high spatial resolution feature representations throughout the entire network. This architectural innovation allows HRNet to preserve fine-grained spatial information essential for pixel-level tasks, while simultaneously integrating multiscale semantic context. As shown in Figure 2, HRNet achieves this by constructing a multi-branch architecture, where parallel subnetworks process the input at different spatial resolutions. Starting with a high spatial resolution stream, lower spatial resolution branches are progressively added in parallel rather than in series. Crucially, instead of isolating these spatial resolution streams, HRNet performs repeated multiscale fusion via continuous information exchange across branches. This "parallel and fusion" design results in high-quality, spatially precise representations that are preserved consistently across all stages of the network.

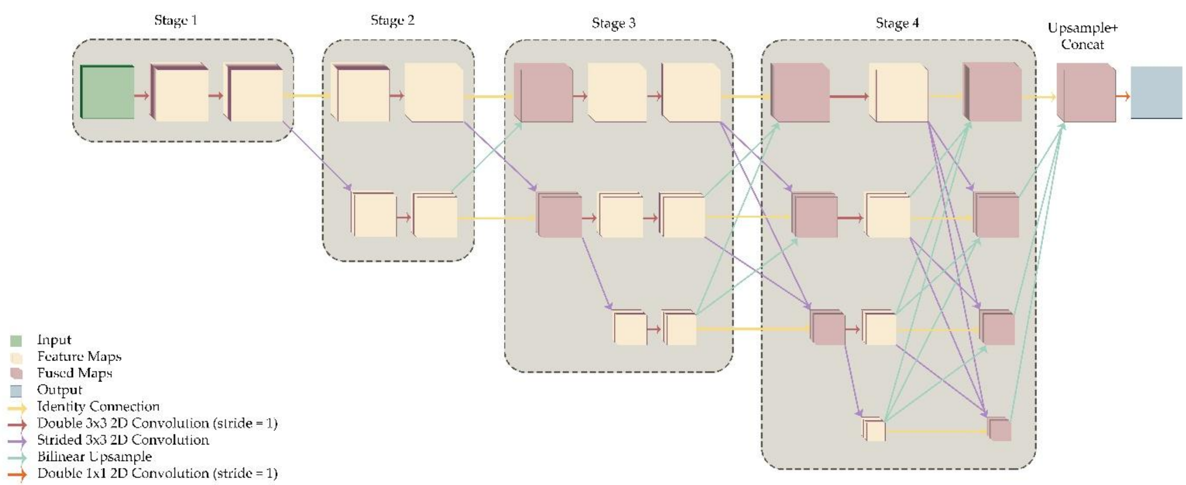

Figure 2. Conceptualization of HRNet architecture [4].

In their foundational paper, Wang et al. [4] demonstrated that HRNet significantly outperforms traditional backbones such as ResNet, as well as advanced segmentation frameworks like DeepLab and PSPNet, across a range of benchmarks including human pose estimation, object detection, and semantic segmentation. Their results highlight HRNet's capacity to retain accurate spatial structures without sacrificing semantic richness, addressing a key limitation of many encoder-decoder models. In semantic segmentation tasks, HRNet's ability to maintain high spatial resolution feature maps and integrate them with multiscale representations leads to sharper object boundaries and more reliable predictions, particularly for fine-scale and elongated structures. This design philosophy makes HRNet especially relevant to remote sensing applications, where both precise object boundaries and multiscale spatial patterns are critical. Several extensions and applications of HRNet demonstrate its advantages in pixel-level prediction. For instance, Sun et al. [28] applied HRNet to pixel labeling tasks and reported superior performance on their specific datasets, noting its ability to produce spatially coherent results. In the remote sensing domain, Cheng and Fu [8] applied HRNet to road and building segmentation and found it outperformed UNet and DeepLabv3+ in both accuracy and mean intersection-over-union (mIoU) across their datasets. Seong and Choi [10] further improved HRNet by incorporating channel and spatial attention gates, which enhanced segmentation performance for irregularly shaped buildings increasing the number of parameters relative to the baseline HRNet.

Recent developments have also focused on improving HRNet's contextual capacity and computational efficiency. Xu et al. [9] proposed HRCNet (high-resolution context extraction network), an HRNet-based model augmented with a dual-branch context extraction module and lightweight fusion strategy, achieving state-of-the-art results by balancing local detail and global context. To address the high resource demands of HRNet, Yu et al. [29] introduced Lite-HRNet, which uses conditional channel weighting and depthwise separable convolutions to reduce computational complexity while maintaining accuracy. Similarly, Zhang et al. [30] proposed HF-HRNet, which simplifies multiscale fusion to improve efficiency while achieving comparable performance with significantly lower FLOPs (floating-point operations per second) and latency. Collectively, these studies highlight the adaptability of HRNet and its derivatives in remote sensing scenarios that demand both spatial precision and computational efficiency. In the context of my study, I explore whether HRNet's high spatial resolution representation learning can yield more accurate and spatially coherent predictions than UNet across various geospatial segmentation tasks.

While previous geomorphic segmentation studies have demonstrated the effectiveness of deep learning architectures, particularly UNet variants, for mapping a range of landforms, several critical gaps remain. Many studies have focused on either natural or anthropogenic features in isolation, often using a single dataset or feature type, which limits their generalizability. Moreover, while terrain-based inputs, such as lidar-derived LSPs, have shown strong potential, few studies have systematically compared how different CNN architectures perform across features with distinct geomorphic signatures, such as the stepped, linear structure of mine benches versus the irregular, concave morphology of sinkholes. Additionally, despite widespread use of UNet, comparatively little attention has been paid to newer architectures like HRNet in terrain-only applications, particularly in relation to sample size sensitivity and computational trade-offs. This study addresses these gaps by comparing UNet and HRNet using consistent lidar-derived inputs, across multiple sample sizes and two fundamentally different landform types, thereby contributing new insights into how architecture and data availability shape segmentation outcomes in terrain-based geospatial analysis.

4. Methods

4.1. Study Areas

Two distinct study areas, subsets shown in Figure 3, were used to evaluate the performance of models in extracting geomorphic features from lidar-derived data: one characterized by anthropogenic mine benches and the other by naturally occurring sinkholes. Both areas are located within West Virginia but represent different geomorphic processes and classification challenges.

Historic mining activity in West Virginia has left a legacy of altered topography, making it an ideal testbed for training deep learning models to identify anthropogenic landforms. The mine benches dataset [31] was created by our lab through manual digitization of lidar-derived topographic data, aerial imagery, and mine disturbance maps. These benches are linear remnants of contour strip mining, conducted prior to the Surface Mining Control and Reclamation Act (SMCRA) of 1977, which mandated that mined lands be returned to approximate original contour. Although many of these sites have been revegetated and are visually obscured, the benches remain clearly detectable in high spatial resolution terrain models due to their distinct geomorphic form. Figure 3(a) shows examples of individual mine benches, while Figure 3(b) illustrates the stack of LSPs created for this study to represent mine benches.

Extracting sinkholes in karst regions is essential for identifying geohazards, protecting groundwater resources, and informing land-use planning. In West Virginia and across the U.S., many communities rely on karst aquifers for drinking water, and undetected sinkholes can lead to ground collapse, structural damage, flooding, and contamination. The sinkhole dataset [32] was developed and provided through a collaboration between the West Virginia GIS Technical Center (WVGISTC) and the West Virginia Department of Environmental Protection (WVDEP). In contrast to the linearity of mine benches, sinkholes exhibit radial symmetry and subtle concave topography, often requiring more sensitive feature detection. Figure 3(c) presents examples of individual sinkholes, and Figure 3(d) shows the corresponding LSP stack used to represent sinkholes in this study.

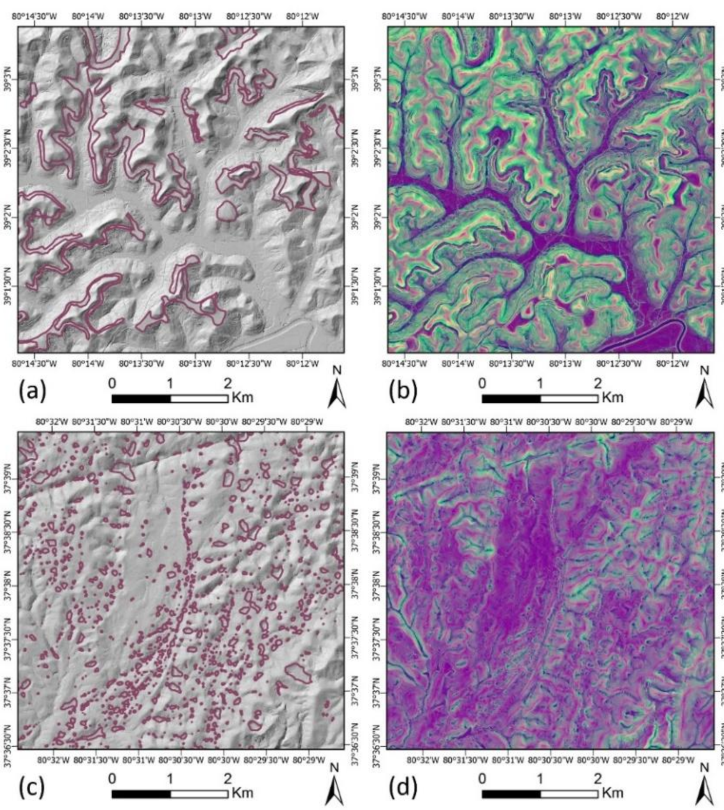

Figure 3. Examples of the geomorphic features and input data used in this study. (a) Individual mine benches extracted within the study area. (b) Stack of LSPs created to represent mine benches. (c) Individual sinkholes extracted within the study area. (d) Stack of LSPs created to represent sinkholes.

4.2. DTMs and LSPs

DTMs, derived from classified lidar point clouds, represent the bare-earth surface by removing vegetation and built structures, enabling precise characterization of bare earth topography and associated geomorphic features. High spatial resolution DTMs serve as the foundational input for generating LSPs used in model training and inference. In this study, I use DTMs sourced from the USGS 3D Elevation Program (3DEP) [33], which provides standardized, quality-controlled datasets. From these DTMs, various LSPs are computed to capture key morphometric characteristics relevant to feature extraction, including slope, aspect, curvature, topographic position index (TPI), and local relief. These parameters enhance the ability of deep learning models to distinguish subtle variations in landform shape, scale, and spatial context, particularly important for detecting features such as mine benches with abrupt slope changes and sinkholes with concave depressions.

Different LSPs have been explored as inputs to deep learning–based workflows for geomorphic mapping. In this study, I employed a modified three-layer terrain feature framework originally developed by Drs. William Odom and Dan Doctor of the USGS, which has been documented by Maxwell et al. [14] to effectively support the extraction of geomorphic features using semantic segmentation. The feature stack (shown in Figure 3(b) and 3(d)) includes the square root of slope (in degrees), which emphasizes moderate to steep terrain gradients while reducing the influence of extreme values. The second layer is a broad-scale TPI, calculated using a 50 m circular moving window to represent general hillslope positions, yielding positive values for ridges and negative values for valleys. The third layer is a fine-scale TPI, computed using an annulus moving window with a 2 m inner and 5 m outer radius, to capture localized surface roughness and small-scale relief features. In both cases, TPI is calculated by subtracting the mean elevation of the surrounding window from the elevation of the center cell, highlighting whether a cell is elevated or depressed relative to its neighborhood. All LSPs were calculated using standardized raster analysis techniques and normalized to ensure comparability across input channels during model training. These calculations were performed in R [34] using the terra [35] and MultiscaleDTM [36] packages.

4.3. Model Training

To train and evaluate the performance of deep learning models for geomorphic feature segmentation, I extracted non-overlapping square image chips from the processed LSP raster grids, as required by CNN-based architectures. Each chip has a spatial size of 512×512 pixels, balancing local context with computational efficiency, a size commonly used in previous geomorphic and remote sensing segmentation studies [6, 7, 37].

As shown in Table 1, for both the mine benches and sinkholes datasets, I constructed three non-overlapping subsets: training, validation, and testing. To evaluate model performance under varying data availability, I trained models using five different training sample sizes: 50, 100, 250, 500, and 1,000. For each sample size, a random subset was selected from the full training pool, while the same validation and testing sets were used across experiments to ensure comparability. This setup allows for assessing model robustness and generalization under limited-data conditions, which are common in real-world geomorphic applications.

Table 1. Overview of the training sample sizes and validation/test chips used for each dataset.

Dataset	Training	Validation	Testing
Mine Benches	50; 100; 250; 500; 1,000	2,334	2,304
Sinkholes	50; 100; 250; 500; 1,000	1,000	1,000

All models were trained and assessed in a Python environment [38] using the PyTorch deep learning framework [39]. The experiments were carried out on a Linux workstation with an AMD Ryzen Threadripper Pro 3955WX 16-core CPU, 128 GB of RAM, and three NVIDIA RTX A5000 GPUs, with a total GPU memory capacity of 72 GB. GPU acceleration through CUDA was used to improve training efficiency. I tested two deep learning architectures: UNet with a standard encoder and HRNet. The base UNet architecture was implemented using PyTorch, specifically the torch and torch.nn modules. The HRNet model was implemented using the original codebase publicly released by its developers [4]. During training, the UNet model generated 16, 32, 64, and 128 feature maps across its four encoder stages, with 256 feature maps in the bottleneck. In the decoder, the feature maps were progressively reduced to 128, 64, 32, and 16, respectively, to reconstruct the spatial resolution and output segmentation maps at the original input size. HRNet maintained high spatial resolution representations across four parallel branches, producing 32, 64, 128, and 256 feature maps at different spatial scales, which were fused at each encoder stage, followed by 256 feature maps in the decoder.

Each model was trained for 25 epochs using a mini-batch size of 12. A modified unified focal Tversky loss, inspired by the implementation in the R-based [34] geodl package [40], was implemented using PyTorch and used as the loss function in this experiment. This loss function was selected because of its effectiveness in addressing class imbalance and improving boundary delineation, both of which are critical challenges in geomorphic feature extraction. I employed the AdamW optimizer with a learning rate of 1e-3 to optimize model weights. To ensure optimal performance, the model achieving the highest F1-score on the validation set during training was selected and saved for final testing. This criterion helps prevent overfitting and ensures better generalization to unseen data.

4.4. Model Assessment

To evaluate the performance of the trained models, I relied on standard classification metrics derived from the confusion matrix, which provides a detailed comparison between predicted and reference pixel classes. This matrix forms the foundation for the evaluation framework and is particularly valuable in geomorphic feature extraction tasks, where class imbalance and subtle spatial patterns often pose significant challenges.

A confusion matrix is a tabular structure that summarizes the outcomes of a classification task by organizing predictions into four categories: true positives (TPs), false positives (FPs), true negatives (TNs), and false negatives (FNs) [41]. In binary classification, this results in a 2×2 matrix (Table 2), where the columns typically represent the reference data and the rows represent the predicted labels. TPs are feature pixels correctly classified as features, while TNs are background pixels correctly identified as background. FPs refer to background pixels that are incorrectly labeled as features (also known as commission errors relative to the positive case), and FNs occur when actual feature pixels are missed by the model and classified as background (known as omission errors relative to the positive case).

Table 2. Conceptualization of the binary confusion matrix.

		Reference Data	
		Positive	Negative
Predicted Labels	Positive	TP	FP
	Negative	FN	TN

The confusion matrix is a valuable tool because it not only reports how many predictions are correct but also reveals what kinds of mistakes the model is making [42, 43]. This is crucial in the context of geomorphic mapping, where features of interest often occupy a small fraction of the total landscape. Without implementing assessments with the confusion matrix, a model could achieve deceptively high accuracy simply by predicting the dominant class and ignoring minority classes.

From the confusion matrix, I derived four key metrics: overall accuracy (OA), precision, recall, and F1-score. Overall accuracy (Equation 1) is the ratio of correctly classified pixels to the total number of pixels. While overall accuracy provides a general performance indicator, it can be misleading when the dataset is imbalanced, as it does not reflect the model's ability to identify less frequent but critical classes. To address this limitation, I also reported precision (Equation 2), which measures the proportion of predicted feature pixels that are correct, and recall (Equation 3), which measures the proportion of actual feature pixels correctly identified. Low precision suggests the model is over-predicting the feature class, resulting in commission errors, while low recall indicates under-prediction and omission errors. To balance these two, I computed the F1-score (Equation 4), the harmonic mean of precision and recall. The F1-score is especially useful when both types of errors carry meaningful consequences, as is often the case in geomorphic applications [11, 12, 44].

$$OA = \frac{\mathrm{TP} + \mathrm{TN}}{\mathrm{TP} + \mathrm{TN} + \mathrm{FP} + \mathrm{FN}} \quad \text{(Equation 1)}$$

$$Precision = \frac{\mathrm{TP}}{\mathrm{TP} + \mathrm{FP}} \quad \text{(Equation 2)}$$

$$Recall = \frac{\mathrm{TP}}{\mathrm{TP} + \mathrm{FN}} \quad \text{(Equation 3)}$$

$$F1 - score = \frac{2 \times \mathrm{Precision} \times \mathrm{Recall}}{\mathrm{Precision} + \mathrm{Recall}} \quad \text{(Equation 4)}$$

These metrics are essential to the evaluation because they collectively capture different aspects of model performance. Overall accuracy gives a high-level snapshot, precision tells us how reliable the model's predictions are, recall reveals the model's sensitivity to detecting actual features, and the F1-score provides a balanced measure that accounts for both types of error. In my experiments, I computed these metrics for each model across all training scenarios and reported them on the held-out test set. Together, these assessments offer a robust, interpretable, and application-relevant framework for evaluating the capability of deep learning models to accurately segment geomorphic features under varying data conditions.

Finally, in addition to accuracy metrics, I reported the number of trainable **parameters, FLOPs**, and MACs for each model configuration. These measures provide insight into the computational cost and efficiency of the architectures, enabling a balanced evaluation of not only model accuracy but also scalability and resource requirements for geomorphic mapping applications. FLOPs quantify the total number of arithmetic operations, such as additions and multiplications, that a model performs during a single forward pass, serving as a hardware-independent proxy for computational cost. MACs count the number of fused multiply-then-add operations, which are the fundamental building blocks of the convolutions and matrix multiplications that dominate deep learning computation. Because each multiply-accumulate consists of one multiplication and one addition, one MAC corresponds to roughly two FLOPs, and the two metrics are therefore closely related. Together with the trainable parameter count, which reflects a model's memory footprint and storage requirements, these measures characterize how demanding each architecture is to train and deploy.

5. Results

This section reports the performance of the baseline UNet and HRNet models for segmenting mine benches and sinkholes from lidar-derived LSPs. The results are organized into four parts: training and validation behavior across epochs; quantitative accuracy on the held-out test sets across the five training sample sizes (50, 100, 250, 500, and 1,000); qualitative comparison of predictions for a test area across the five training sample sizes; and model computational efficiency. Together, these results provide the basis for evaluating the three hypotheses introduced in the Research Objectives above: the expected overall advantage of HRNet (H1), the dependence of relative performance on feature type (H2), and the influence of training sample size on each architecture (H3).

5.1. Training and Validation Behavior

The training loss curves for both architectures are shown in Figure 4, and the corresponding validation F1-scores recorded over the 25 training epochs are shown in Figure 5. For both mine benches and sinkholes, the training loss for UNet and HRNet decreased rapidly during the first several epochs before gradually flattening, indicating stable convergence under the unified focal Tversky loss and the AdamW optimizer. As expected, configurations trained with larger sample sizes achieved lower final training loss and reached more stable plateaus, while the smallest sample sizes (50 and 100 chips) exhibited noisier loss trajectories and greater epoch-to-epoch fluctuation, consistent with the limited diversity of the training pool. Neither architecture showed signs of divergence or unstable training across any of the sample-size configurations.

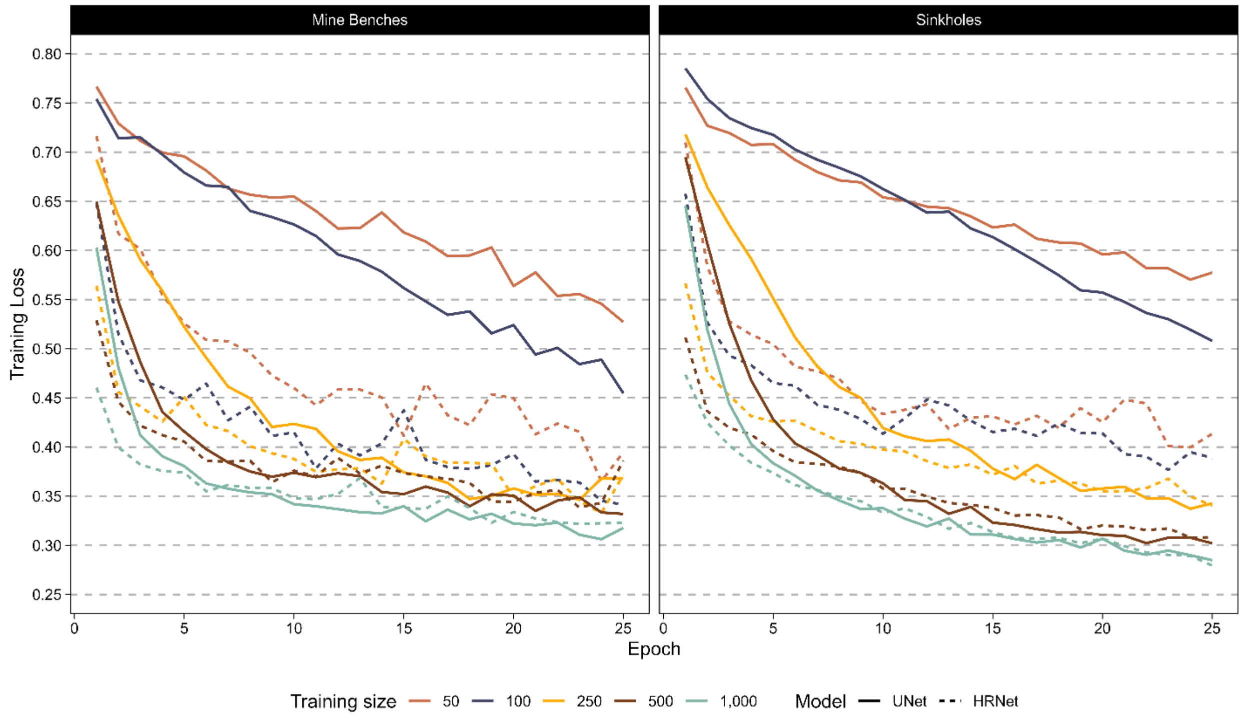

Figure 4. Training loss curves for the UNet and HRNet models across the five training sample sizes (50, 100, 250, 500, and 1,000) for the sinkhole and mine bench datasets.

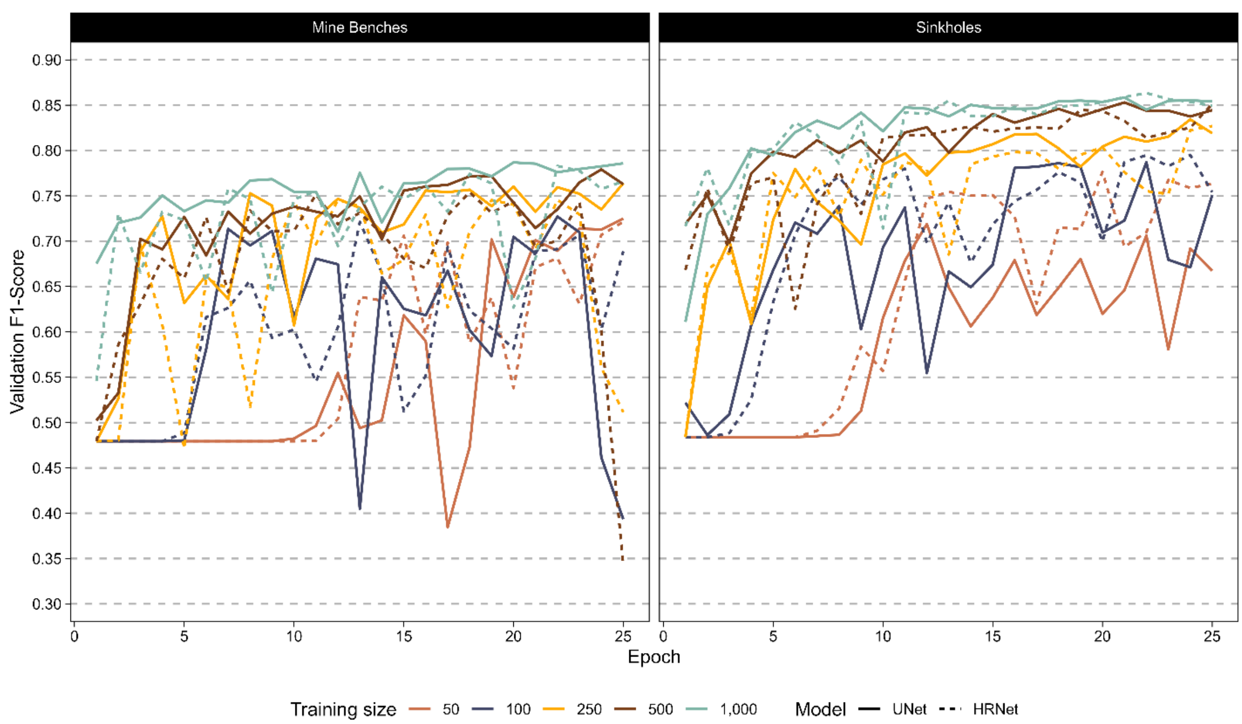

Figure 5. Validation F1-score curves for the UNet and HRNet models across the five training sample sizes (50, 100, 250, 500, and 1,000) for the sinkhole and mine bench datasets.

The validation F1-score curves (Figure 5) followed a complementary pattern, rising steeply in the early epochs and then stabilizing. Because the model achieving the highest validation F1-score was retained for final testing, these curves also illustrate the basis for model selection. Validation performance improved generally with larger training sample sizes for both architectures and both feature types. At the smallest sample sizes, the validation curves were more variable, reflecting greater sensitivity to the particular chips included in the limited training subsets. Overall, the training and validation behavior confirms that both models were trained successfully and that the model selection criterion produced stable, well-converged models for the subsequent test-set evaluation.

5.2. Test-Set Accuracy Across Sample Sizes

Test-set F1-scores for both architectures across all five training sample sizes are summarized in Figure 6, and the complete set of accuracy metrics, including overall accuracy, F1-score, precision, and recall, is reported in Table 3. Because the feature classes occupy only a small fraction of each scene, F1-score is emphasized here as the primary metric, as it balances commission and omission errors and is more informative than overall accuracy under class imbalance.

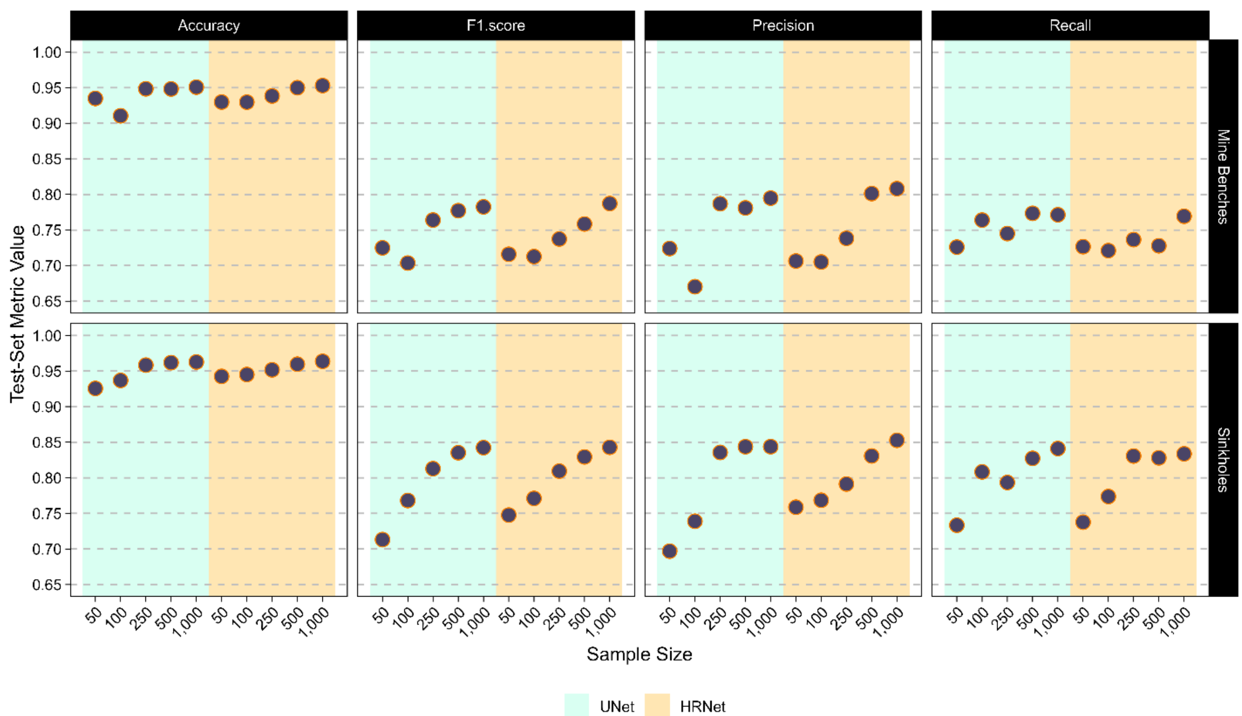

Figure 6. Test-set performance metrics (overall accuracy, F1-score, precision, and recall) as a function of training sample size for the UNet and HRNet models on the sinkhole and mine bench datasets.

Across both feature types, the two architectures produced broadly comparable test-set accuracy, and performance generally improved as the training sample size increased. For sinkholes, F1-scores rose from 0.7132 (UNet) and 0.7476 (HRNet) at 50 training chips to 0.8424 (UNet) and 0.8429 (HRNet) at 1,000 chips. For mine benches, F1-scores increased from 0.7250

(UNet) and 0.7159 (HRNet) at 50 chips to 0.7826 (UNet) and 0.7872 (HRNet) at 1,000 chips. Overall accuracy was high in every configuration (0.91 to 0.96), but, as anticipated for imbalanced classes, it varied far less than F1-score and therefore offers limited discrimination between models; the F1-score, precision, and recall values provide a more meaningful basis for comparison.

Table 3. Test-set performance of the UNet and HRNet models for the sinkhole and mine bench segmentation problems across the five training sample sizes. The largest metric achieved is bolded for each use case.

Problem	Model	Size	Accuracy	F1-score	Precision	Recall
Sinkholes	UNet	50	0.9256	0.7132	0.6969	0.7334
		100	0.9369	0.7681	0.7389	0.8083
		250	0.9584	0.8128	0.8356	0.7934
		500	0.9619	0.8353	0.8437	0.8273
		1000	0.9628	0.8424	0.8438	**0.8411**
	HRNet	50	0.9426	0.7476	0.7587	0.7377
		100	0.9452	0.7710	0.7684	0.7737
		250	0.9517	0.8094	0.7913	0.8306
		500	0.9597	0.8294	0.8307	0.8280
		1000	**0.9637**	**0.8429**	**0.8527**	0.8337
Mine Benches	UNet	50	0.9350	0.7250	0.7240	0.7260
		100	0.9106	0.7036	0.6704	0.7639
		250	0.9485	0.7640	0.7870	0.7450
		500	0.9482	0.7772	0.7811	**0.7734**
		1000	0.9508	0.7826	0.7949	0.7714
	HRNet	50	0.9298	0.7159	0.7065	0.7266
		100	0.9297	0.7127	0.7051	0.7210
		250	0.9384	0.7374	0.7383	0.7365
		500	0.9500	0.7585	0.8012	0.7279
		1000	**0.9530**	**0.7872**	**0.8081**	0.7694

Contrary to the expectation in H1 that HRNet would outperform UNet across both feature types, neither architecture established a consistent advantage. At the largest sample size, the two models were nearly indistinguishable: for sinkholes at 1,000 chips, HRNet attained a marginally higher F1-score (0.8429 versus 0.8424), while for mine benches at 1,000 chips, HRNet was again slightly higher (0.7872 versus 0.7826). At intermediate sample sizes, however, UNet frequently matched or exceeded HRNet. For sinkholes, UNet produced higher F1-scores at 250 and 500 chips (0.8128 and 0.8353 versus 0.8094 and 0.8294), and for mine benches, UNet led at 50, 250, and 500 chips. These differences are small in absolute terms and indicate near-parity rather than a clear advantage for either architecture under the terrain-only, baseline configuration used here. One possible explanation for HRNet's lower performance relative to UNet at some of the smaller sample sizes is overfitting, given HRNet's substantially larger parameter count.

The clearest distinction between the architectures emerged at the smallest sample size and varied by feature type, which bears directly on H2 and H3. For sinkholes trained using only 50 chips, HRNet showed a practically notable advantage over UNet, with an F1-score of 0.7476 compared to 0.7132 for UNet, a difference of approximately 3.4 percentage points. This suggests that HRNet's continuously maintained high-resolution representations were advantageous for detecting small, radially symmetric, concave sinkhole features when training data were limited.

For mine benches at 50 chips, the pattern reversed modestly, with UNet slightly ahead (0.7250 versus 0.7159). This result does not fully support H2. H2 predicted that HRNet would perform better for irregular sinkholes, while UNet would be more competitive for structured mine benches. However, the results showed a different pattern. Feature type did affect the relative performance of the two models, but HRNet's advantage was strongest for sinkholes only when the training sample size was very small. At larger sample sizes, the two models performed similarly for mine benches. This result also adds nuance to H3. HRNet did not consistently overfit when training data were limited. Instead, HRNet was more robust than UNet for sinkholes at the smallest sample size, while both models showed similar stability for mine benches.

Examining precision and recall provides additional insight into the nature of each model's errors. At the largest sample size, HRNet tended to favor precision over recall more strongly than UNet. For mine benches at 1,000 chips, HRNet achieved higher precision (0.8081 versus 0.7949) but slightly lower recall (0.7694 versus 0.7714), and a similar precision-leaning balance appeared for sinkholes (precision 0.8527 and recall 0.8337 for HRNet, compared with the more evenly balanced 0.8438 and 0.8411 for UNet). This indicates that HRNet was marginally more conservative, producing fewer commission errors at the cost of slightly more omission, whereas UNet produced more balanced commission and omission errors. Mine benches were also consistently more difficult than sinkholes for both architectures, with mine bench F1-scores plateauing near 0.78 to 0.79 while sinkhole F1-scores reached approximately 0.84, reflecting the greater challenge of delineating the elongated, linear bench features relative to the more compact sinkhole depressions.

5.3. Qualitative Comparison of Predictions

To complement the quantitative metrics, representative predictions from both architectures are shown for mine benches in Figure 7 and for sinkholes in Figure 8. The visual results are consistent with the numerical findings: both UNet and HRNet captured the overall extent and location of the target features, and the predicted masks generally aligned well with the reference labels. For mine benches, both models successfully traced the elongated, stepped structure of the benches, though some fragmentation and boundary imprecision appeared along the thinnest segments, in keeping with the lower F1-scores observed for this feature type. For sinkholes, both models delineated the compact, concave depressions with clean boundaries, and predictions improved in completeness and boundary sharpness as the training sample size increased. Differences between the two architectures were subtle and did not reveal a consistent qualitative advantage for either model, mirroring the near-parity seen in Table 3.

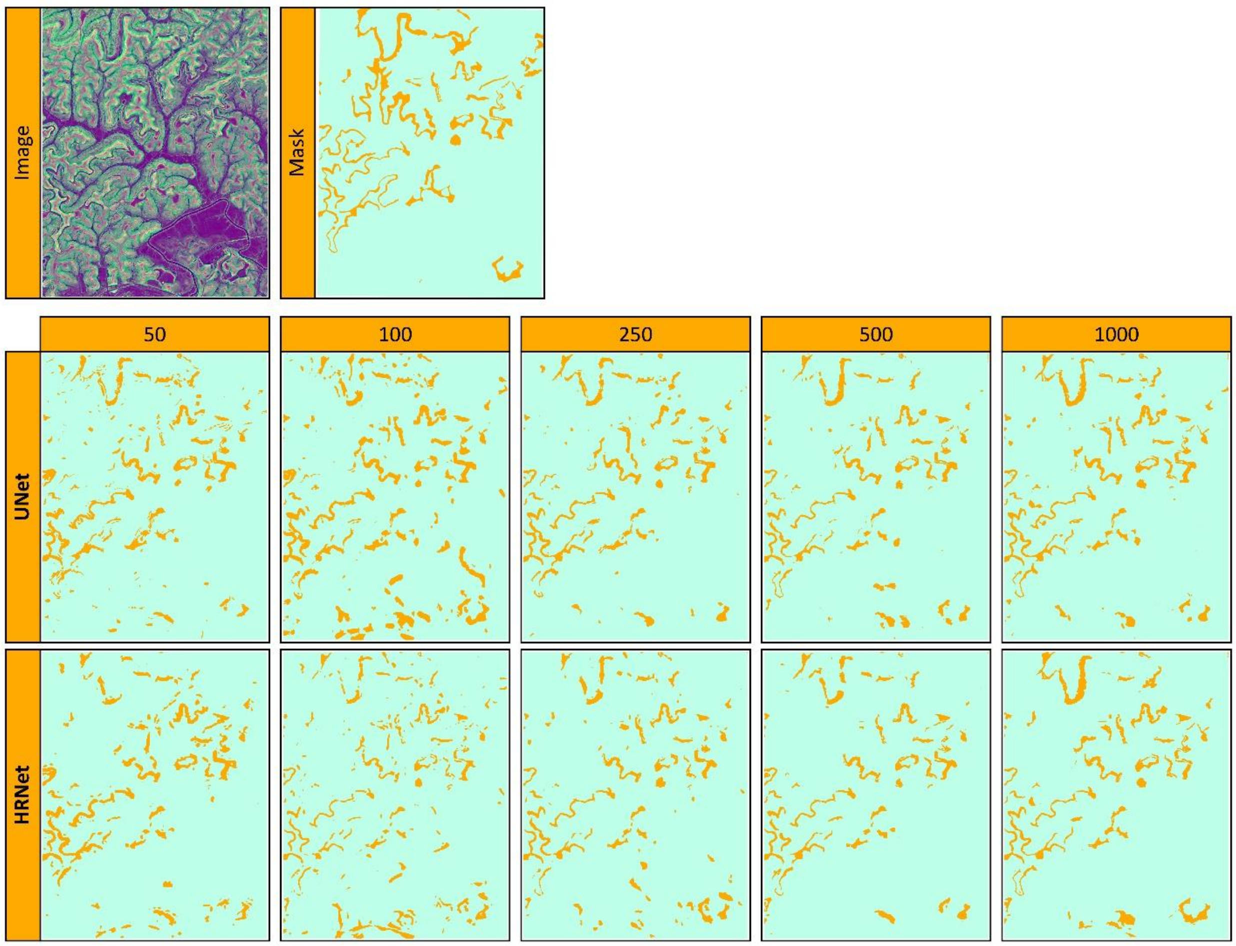

Figure 7. Qualitative comparison of UNet and HRNet mine bench predictions across training sample sizes, shown with the input image and reference mask.

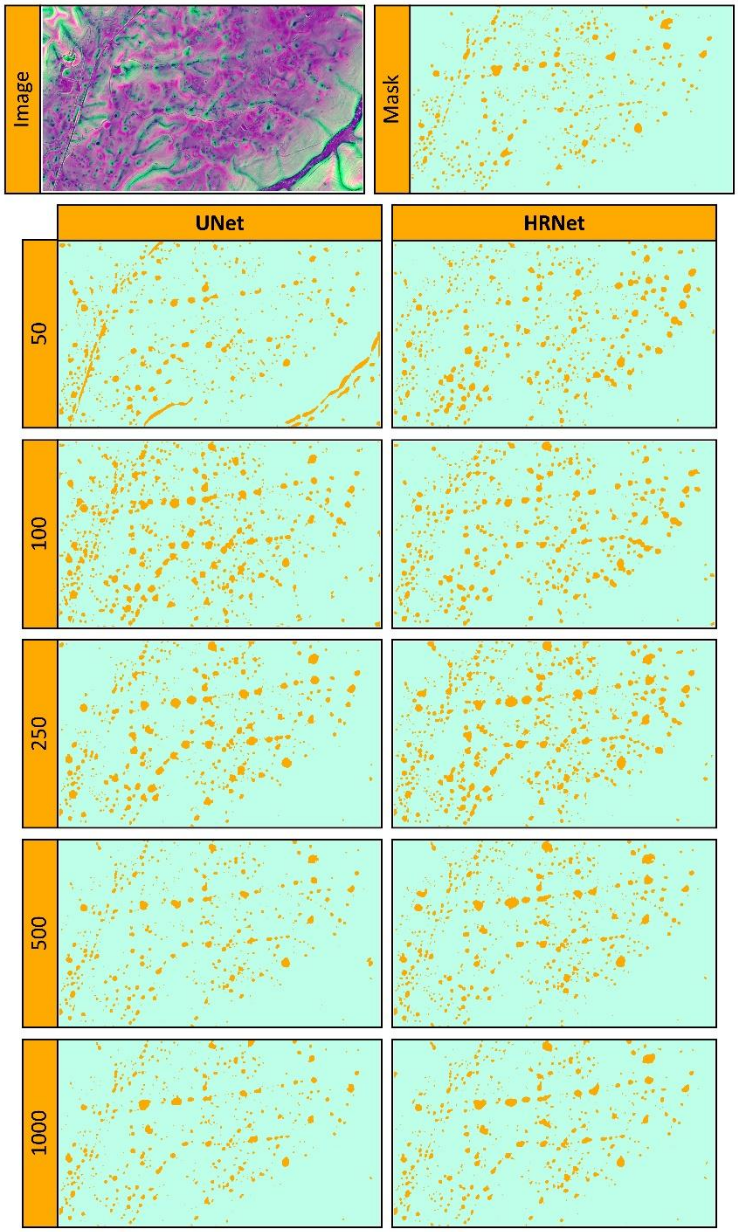

Figure 8. Qualitative comparison of UNet and HRNet sinkhole predictions across training sample sizes, shown with the input image and reference mask.

5.4. Model Efficiency

The computational cost of the two architectures differed substantially, as summarized in Table 4. UNet was far more lightweight, with approximately 2.32 million trainable parameters, 364.9 GFLOPs, and 181.04 GMACs. HRNet was considerably larger and more demanding, with roughly 29.54 million trainable parameters, 1.08 TFLOPs, and 540.23 GMACs. In relative terms, HRNet required about 12.7 times as many trainable parameters and roughly three times the FLOPs and MACs of UNet for the same input. This large disparity in computational cost did not translate into a corresponding accuracy advantage: as shown in Table 3, HRNet's test-set F1-scores were at best marginally higher than UNet's and were lower in several configurations. UNet therefore achieved comparable accuracy at a small fraction of the parameter count and computational burden, an important consideration for deployment in resource-constrained settings or for scaling inference across large geographic areas.

Table 4. Computational complexity of the UNet and HRNet models in terms of trainable parameters, FLOPs, and MACs.

Model	Trainable Parameters	FLOPs	MACs
UNet	2.32 M	364.9 GFLOPs	181.04 GMACs
HRNet	29.54 M	1.08 TFLOPs	540.23 GMACs

6. Discussion

This study aimed to compare baseline UNet and HRNet architectures for the semantic segmentation of two contrasting geomorphic feature types, mine benches and sinkholes, using only lidar-derived land surface parameters as input, and to examine how their relative performance changed with training sample size and computational cost. The results offer a nuanced picture that only partially aligns with the study's initial hypotheses and, in several respects, challenges the assumption that a more complex, larger, and advanced architecture necessarily yields better terrain-based segmentation.

6.1. Overall Architecture Performance (H1)

The first hypothesis (H1) predicted that HRNet would outperform UNet in segmentation accuracy across both feature types, owing to its continuous maintenance of high-resolution representations and repeated multiscale fusion. The results do not support this expectation. Across the five sample sizes and two feature types, the two architectures performed at near-parity, with F1-score differences typically within one to three percentage points. HRNet held a slight edge at the largest sample size for both features, but UNet matched or exceeded HRNet at several intermediate sample sizes. The absence of a decisive HRNet advantage suggests that, for terrain-only inputs composed of a small number of smoothly varying land surface parameters, the additional representational capacity of HRNet does not provide the same benefit that has been reported for high-resolution optical or multispectral imagery, where fine texture and spectral richness reward the preservation of high-resolution feature maps. When the input signal is a compact, three-layer terrain stack, UNet's encoder-decoder design with skip connections appears sufficient to recover the spatial detail needed to delineate these features.

This finding is consistent with prior work in our lab demonstrating that carefully configured UNet models trained on terrain-derived inputs can extract anthropogenic geomorphic features with high accuracy [6, 7, 45]. It also echoes a broader theme in the segmentation literature: architectural innovations that prove decisive on natural-image benchmarks do not always transfer to specialized geospatial domains, where input characteristics, class imbalance, and feature morphology differ substantially from the conditions under which those architectures were originally optimized.

6.2. Feature-Type Dependence (H2)

The second hypothesis (H2) anticipated that model performance would vary by feature type, with HRNet showing particular advantages for irregular, fine-scale sinkholes and UNet remaining competitive on structured mine benches. The results support the general premise that relative performance depends on feature type, but the specific direction was more complex than predicted. HRNet's clearest advantage over UNet appeared for sinkholes, but only at the smallest training sample size, where it exceeded UNet by roughly three F1-score percentage points. As sample size increased, this advantage disappeared and the two models converged. For mine benches, the two architectures were essentially tied across most configurations, with UNet slightly ahead at several sample sizes. Thus, rather than a clean split in which HRNet owned the irregular features and UNet owned the structured ones, the feature-type effect manifested mainly as a data-efficiency advantage for HRNet on sinkholes under scarce data.

A plausible explanation lies in the morphology of the two feature types. Sinkholes are small, compact, radially symmetric depressions whose topographic signature is concentrated in a limited spatial footprint; HRNet's continuously high-resolution branches may help localize these subtle, concentrated depressions when only a few training examples are available. Mine benches, by contrast, are elongated, linear features whose extended geometry is well captured by UNet's multiscale encoder-decoder pathway and skip connections. Both feature types also proved differentially difficult overall: sinkhole F1-scores reached approximately 0.84, whereas mine bench F1-scores plateaued near 0.78 to 0.79 for both models, indicating that the thin, linear bench features are inherently harder to delineate precisely regardless of architecture.

The broader geologic and geomorphic setting also provides additional context for interpreting these results. The sinkhole dataset is concentrated primarily within the Greenbrier Valley, where the relatively flat-lying Greenbrier Limestone supports extensive karst development and abundant sinkholes with relatively consistent closed-depression morphology. In contrast, the mine bench dataset spans a much larger geographic area containing multiple Pennsylvanian-age rock units, different coal seams, and varied mining histories. Consequently, the greater variability observed for mine benches is likely influenced not only by geology, but also by differences in mining methods, reclamation history, feature age, vegetation, and local topographic complexity. Together, these interacting factors produce greater variation in bench morphology than is present in the sinkhole dataset, making mine benches inherently more challenging to segment consistently.

6.3. Sample Size Sensitivity (H3)

The third hypothesis (H3) predicted that both models would benefit from larger training samples, and that HRNet's greater architectural complexity might lead to overfitting under limited data while UNet's simpler design offered greater stability. The first part of this hypothesis was clearly confirmed: F1-scores increased monotonically, or nearly so, with training sample size for both architectures and both feature types, and the largest gains occurred between the smallest sample sizes. This underscores that data availability remains a primary driver of performance in terrain-based geomorphic segmentation, often outweighing the choice of architecture.

The second part of H3, however, was not supported. HRNet did not exhibit the anticipated overfitting under limited data. On the contrary, for sinkholes at 50 training chips, HRNet was the more robust model, showing a practically notable advantage over UNet, and it remained stable rather than degrading at small sample sizes. For mine benches, the two architectures were comparably stable when data were scarce. The expectation that a larger model would necessarily be more prone to overfitting therefore did not hold in this terrain-only setting, at least within the range of sample sizes tested. One contributing factor may be the use of validation-based model selection, which retained the checkpoint with the highest validation F1-score and thereby mitigated overfitting for both architectures.

6.4. Accuracy–Efficiency Trade-offs

Perhaps the most practically consequential finding concerns the relationship between accuracy and computational cost. HRNet required roughly 12.7 times as many trainable parameters as UNet and about three times the FLOPs and MACs, yet delivered accuracy that was, at best, marginally higher and frequently equivalent or lower. From an applied standpoint, this represents a substantial efficiency advantage for UNet. For geomorphic mapping tasks that must scale across large geographic extents, run on modest hardware, or support rapid iteration and retraining, UNet offers comparable accuracy at a small fraction of the computational burden. HRNet's additional cost would only be justified in scenarios where its narrow data-efficiency advantage on certain feature types under very limited training data is decisive, or where future tuning unlocks accuracy gains not realized by the baseline configuration evaluated here.

6.5. Limitations and Future Work

Several limitations should temper the interpretation of these results. First, both models were evaluated in baseline configurations with a fixed training budget of 25 epochs, a single loss function, and identical hyperparameters chosen to ensure a fair comparison. It is possible that HRNet, which has a larger capacity, would benefit more than UNet from extended training, architecture-specific hyperparameter tuning, pretraining, or data augmentation, and that its full potential was not realized under these controlled conditions. Second, the evaluation covered two feature types within West Virginia, and although these represent contrasting morphologies, generalization to other landforms, regions, and lidar acquisition characteristics remains to be tested. Finally, the comparison considered only the baseline UNet and HRNet; lighter-weight HRNet variants and modern UNet derivatives were outside the scope of this work.

Another limitation is that terrain morphology alone cannot always distinguish target landforms from other features with similar topographic expression. For example, road cuts, terraced highway slopes, construction sites, and other elongated flat surfaces may resemble mine benches, while artificial excavations, drainage features, ponds, or depressions associated with land development may resemble sinkholes. Because this study relied exclusively on lidar-derived land surface parameters, no ancillary datasets, such as road networks, coal seam maps, land cover, or geologic information, were incorporated to help reduce these ambiguities. In addition, uncertainty within the reference datasets, including manually digitized mine bench boundaries and mapped sinkhole extents, may have influenced the reported accuracy, particularly along feature boundaries.

These limitations point to clear directions for future research. Promising avenues include evaluating architecture-specific training and augmentation strategies, exploring transfer learning and pretraining for both models, extending the comparison to additional geomorphic feature types and study regions, and assessing efficiency-oriented variants such as Lite-HRNet alongside residual or attention-augmented UNet designs. Such work would clarify whether the near-parity observed here persists under more favorable conditions for HRNet or whether UNet's efficiency advantage holds across a broader range of terrain-based segmentation tasks.

Future research should also investigate how model performance varies across different geologic settings and geomorphic conditions. Evaluating mine benches representing different mining eras, reclamation histories, and weathering stages would help determine how well the models generalize to landscapes with varying geomorphic expression. In addition, incorporating ancillary spatial datasets, such as road networks, coal seam maps, land-cover information, or geologic maps, either as additional model inputs or during post-processing, may reduce false-positive predictions and further improve segmentation accuracy.

7. Conclusion

This study compared baseline UNet and HRNet deep learning models for the semantic segmentation of two contrasting geomorphic feature types, mine benches and sinkholes, using only lidar-derived land surface parameters and evaluating performance across five training sample sizes and a range of computational efficiency measures. The central conclusion is that, for terrain-only geomorphic feature extraction, the two architectures performed at near-parity, and the substantial additional complexity of HRNet did not yield a corresponding accuracy advantage over the much lighter UNet.

Relative to the study's hypotheses, the evidence did not support a uniform HRNet advantage (H1), only partially supported a feature-type dependence (H2) in the form of a data-efficiency benefit for HRNet on sinkholes under scarce data, and confirmed the strong influence of sample size (H3) while contradicting the prediction that HRNet would overfit more readily under limited data. Across both feature types, performance improved markedly with larger training samples, sinkholes were segmented more accurately than the thin, linear mine benches, and HRNet adopted a slightly more precision-leaning error balance than the more evenly balanced UNet.

Taken together, these findings indicate that, in the absence of architecture-specific tuning and with compact terrain-derived inputs, the lightweight UNet is a highly competitive and computationally efficient choice for geomorphic feature extraction, achieving accuracy comparable to HRNet at a fraction of the parameters and computational cost. HRNet retains potential value where its data-efficiency advantage on certain feature types is important or where further optimization can unlock additional accuracy. More broadly, the results reinforce that data availability and feature morphology are at least as influential as architectural choice in terrain-based geospatial segmentation, and they provide practical guidance for selecting and deploying deep learning models in geomorphic hazard monitoring, terrain change analysis, and environmental regulation compliance.

References

1. Ali, M., et al., *Slope Instability Below Historic Mine Benches in the Northern Coalfields of West Virginia.* Environmental & Engineering Geoscience, 2025.
2. Gutiérrez, F., A.H. Cooper, and K.S. Johnson, *Identification, prediction, and mitigation of sinkhole hazards in evaporite karst areas.* Environmental Geology, 2008. **53**(5): p. 1007-1022.
3. Ronneberger, O., P. Fischer, and T. Brox. *U-Net: Convolutional Networks for Biomedical Image Segmentation*. in *Medical Image Computing and Computer-Assisted Intervention – MICCAI 2015*. 2015. Cham: Springer International Publishing.
4. Wang, J., et al., *Deep High-Resolution Representation Learning for Visual Recognition.* IEEE Transactions on Pattern Analysis and Machine Intelligence, 2021. **43**(10): p. 3349-3364.
5. Maxwell, A.E., et al. *Semantic Segmentation Deep Learning for Extracting Surface Mine Extents from Historic Topographic Maps*. Remote Sensing, 2020. **12**, DOI: 10.3390/rs12244145.
6. Maxwell, A.E., S. Farhadpour, and M. Ali *Exploring Transfer Learning for Anthropogenic Geomorphic Feature Extraction from Land Surface Parameters Using UNet*. Remote Sensing, 2024. **16**, DOI: 10.3390/rs16244670.
7. Farhadpour, S. and A.E. Maxwell, *Comparing UNet configurations for anthropogenic geomorphic feature extraction from land surface parameters.* PLOS ONE, 2025. **20**(6): p. e0325904.
8. Cheng, Z. and D. Fu. *Remote Sensing Image Segmentation Method based on HRNET*. in *IGARSS 2020 - 2020 IEEE International Geoscience and Remote Sensing Symposium*. 2020.
9. Xu, Z., et al. *HRCNet: High-Resolution Context Extraction Network for Semantic Segmentation of Remote Sensing Images*. Remote Sensing, 2021. **13**, DOI: 10.3390/rs13010071.
10. Seong, S. and J. Choi *Semantic Segmentation of Urban Buildings Using a High-Resolution Network (HRNet) with Channel and Spatial Attention Gates*. Remote Sensing, 2021. **13**, DOI: 10.3390/rs13163087.
11. Maxwell, A.E., T.A. Warner, and L.A. Guillén, *Accuracy Assessment in Convolutional Neural Network-Based Deep Learning Remote Sensing Studies—Part 1: Literature Review.* Remote Sensing, 2021. **13**(13): p. 2450.
12. Maxwell, A.E., T.A. Warner, and L.A. Guillén, *Accuracy Assessment in Convolutional Neural Network-Based Deep Learning Remote Sensing Studies—Part 2: Recommendations and Best Practices.* Remote Sensing, 2021. **13**(13): p. 2591.
13. Maxwell, A.E., P. Pourmohammadi, and J.D. Poyner *Mapping the Topographic Features of Mining-Related Valley Fills Using Mask R-CNN Deep Learning and Digital Elevation Data*. Remote Sensing, 2020. **12**, DOI: 10.3390/rs12030547.
14. Maxwell, A.E., et al., *Exploring the Influence of Input Feature Space on CNN-Based Geomorphic Feature Extraction From Digital Terrain Data.* Earth and Space Science, 2023. **10**(5): p. e2023EA002845.
15. Tarolli, P., et al., *From features to fingerprints: A general diagnostic framework for anthropogenic geomorphology.* Progress in Physical Geography: Earth and Environment, 2019. **43**(1): p. 95-128.
16. Müller, L., et al., *Airborne laser scanning change detection for quantifying geomorphological processes in high mountain regions.* ISPRS Annals of the Photogrammetry, Remote Sensing and Spatial Information Sciences, 2022. **2**: p. 391-398.

17. Ahmad, N., et al. *Characterization and Geomorphic Change Detection of Landslides Using UAV Multi-Temporal Imagery in the Himalayas, Pakistan*. Land, 2024. **13**, DOI: 10.3390/land13070904.
18. Conley, T., S. Hurst, and E. Johnson *Topographic Thresholds and Soil Preservation along the Southern High Plains Eastern Escarpment, Northwest Texas, USA*. Geosciences, 2020. **10**, DOI: 10.3390/geosciences10120476.
19. Chen, X., et al., *Topographic Controls on the Distribution of Coseismic Landslides: A Case Study Using the Coefficient of Variation of the 2014 Ludian, Yunnan, China, Ms6.5 Earthquake.* Lithosphere, 2022. **2021**(Special 2): p. 6678652.
20. van der Meij, W.M., et al., *Comparing geomorphological maps made manually and by deep learning.* Earth Surface Processes and Landforms, 2022. **47**(4): p. 1089-1107.
21. Prakash, N., A. Manconi, and S. Loew *Mapping Landslides on EO Data: Performance of Deep Learning Models vs. Traditional Machine Learning Models*. Remote Sensing, 2020. **12**, DOI: 10.3390/rs12030346.
22. Yi, Y., et al. *Semantic Segmentation of Urban Buildings from VHR Remote Sensing Imagery Using a Deep Convolutional Neural Network*. Remote Sensing, 2019. **11**, DOI: 10.3390/rs11151774.
23. Pan, Z., et al. *Deep Learning Segmentation and Classification for Urban Village Using a Worldview Satellite Image Based on U-Net*. Remote Sensing, 2020. **12**, DOI: 10.3390/rs12101574.
24. He, H., et al. *Road Extraction by Using Atrous Spatial Pyramid Pooling Integrated Encoder-Decoder Network and Structural Similarity Loss*. Remote Sensing, 2019. **11**, DOI: 10.3390/rs11091015.
25. Baumhoer, C.A., et al. *Automated Extraction of Antarctic Glacier and Ice Shelf Fronts from Sentinel-1 Imagery Using Deep Learning*. Remote Sensing, 2019. **11**, DOI: 10.3390/rs11212529.
26. Freudenberg, M., et al. *Large Scale Palm Tree Detection in High Resolution Satellite Images Using U-Net*. Remote Sensing, 2019. **11**, DOI: 10.3390/rs11030312.
27. Onojeghuo, A.O., Y. Miao, and G.A. Blackburn *Deep ResU-Net Convolutional Neural Networks Segmentation for Smallholder Paddy Rice Mapping Using Sentinel 1 SAR and Sentinel 2 Optical Imagery*. Remote Sensing, 2023. **15**, DOI: 10.3390/rs15061517.
28. Sun, K., et al., *High-Resolution Representations for Labeling Pixels and Regions.* ArXiv, 2019. **abs/1904.04514**.
29. Yu, C., et al. *Lite-HRNet: A Lightweight High-Resolution Network*. in *2021 IEEE/CVF Conference on Computer Vision and Pattern Recognition (CVPR)*. 2021.
30. Zhang, H., et al., *HF-HRNet: A Simple Hardware Friendly High-Resolution Network.* IEEE Transactions on Circuits and Systems for Video Technology, 2024. **34**(8): p. 7699-7711.
31. Maxwell, A., S. Farhadpour, and M. Ali, *mineBenchDL: A geomorphology deep learning dataset of historic surface coal mine benches in West Virginia, USA*. 2024, figshare.
32. Center, W.V.G.T., *Sinkholes, https://wvgis.wvu.edu/data/dataset.php?ID=518*. 2025.
33. Sugarbaker, L.J., et al., *The 3D Elevation Program initiative: a call for action*. 2014, US Geological Survey.

34. R Core Team., *R: A Language and Environment for Statistical Computing*. 2022, R Foundation for Statistical Computing, Vienna, Austria.
35. Hijmans, R.J. *terra: Spatial Data Analysis*. 2024 2024]; R package version 1.7-78]. Available from: https://CRAN.R-project.org/package=terra.
36. Ilich, A., et al., *MultiscaleDTM: Multi-Scale Geomorphometric Terrain Attributes (v0.8.3). Zenodo*. 2024.
37. Maggiori, E., et al., *Convolutional neural networks for large-scale remote-sensing image classification.* IEEE Transactions on geoscience and remote sensing, 2016. **55**(2): p. 645-657.
38. *Welcome to Python.org [WWW Document], n.d.* https://www.python.org/ (accessed 1.5.21).
39. *PyTorch [WWW Document], n.d.* https://www.pytorch.org (accessed 12.31.20).
40. Maxwell, A., S. Farhadpour, and S. Das, *geodl: An R package for geospatial deep learning semantic segmentation using torch and terra.* EarthArXiv eprints, 2024.
41. Warner, T.A., M.D. Nellis, and G.M. Foody, *The SAGE Handbook of Remote Sensing*. 2009: 55 City Road, London.
42. Congalton, R. and K. Green, *Assessing the Accuracy of Remotely Sensed Data: Principles and Practices, Third Edition*. 2019.
43. Stehman, S.V., G.M. Foody, and others, *The SAGE Handbook of Remote Sensing*. 2009, SAGE Publications, Inc.: 55 City Road

55 City Road, London.

44. Farhadpour, S., T.A. Warner, and A.E. Maxwell *Selecting and Interpreting Multiclass Loss and Accuracy Assessment Metrics for Classifications with Class Imbalance: Guidance and Best Practices*. Remote Sensing, 2024. **16**, DOI: 10.3390/rs16030533.
45. Maxwell, A.E., S. Farhadpour, and M.M. Reed, *A deep learning architecture and workflow for geomorphic feature extraction using digital terrain model-derived land surface parameters.* Earth Surface Processes and Landforms, 2026. **51**(5): p. e70295.